Catalysis Science & Technology

PAPER

View Article Online
View Journal | View Issue

Cite this: *Catal. Sci. Technol.*, 2016, **6**, 3950

Oxygen vacancies on nanosized ceria govern the NO_x storage capacity of NSR catalysts†

Yan Zhang,‡ Yunbo Yu‡ and Hong He*

Received 30th September 2015,
Accepted 5th January 2016

DOI: 10.1039/c5cy01660f

www.rsc.org/catalysis

$Pt/BaO/CeO_2$ catalysts derived from CeO_2 nanomaterials with shapes of rods, cubes, and particles were investigated for NO_x storage/reduction. Catalytic tests were performed in a transient flow reactor system. A series of characterization techniques including XRD, TEM, XPS, EXAFS, NO_x-TPD, H_2-TPR and *in situ* DRIFTS were conducted to investigate the electrical, chemical, and structural properties. The NO_x storage-reduction performance ranked by the CeO_2 support was nanorods > nanoparticles > nanocubes. Amazingly, the CeO_2-nanorod based NSR catalyst possessed a superior NO_x storage capacity (NSC) of 913.8 μmol NO_x g_{cat}^{-1} at 350 °C in the absence of H_2O and CO_2, which almost reached the theoretical value. Even under harsh lean–rich cycling conditions (90 s *vs.* 6 s) and a high GHSV of 360 000 h^{-1}, the nanorod-based catalyst also showed the best reduction efficiency, affording ~ 99% NO_x conversion levels from 200 °C to 400 °C under the conditions without H_2O and CO_2. The morphology of ceria has significant influences on the selectivity of ammonia, and on the H_2O and CO_2 tolerance during the NSR process. For the first time, a close linear correlation was drawn between the NO_x storage capacity and the amount of oxygen vacancies of NSR catalysts. Over the NSR catalysts, oxygen vacancies play a crucial role in anchoring Pt. Meanwhile, H_2-TPR results showed that the number of active surface oxygen species trapped in oxygen vacancies was closely related to the NSC value. This suggests that the oxygen vacancies on the NSR surface govern the NO_x storage capacity by creating efficient sites or channels for the formation of nitrate and its further transformation to Ba-based storage sites. These findings may be fundamental for designing ceria-based NSR catalysts with better performance.

Introduction

Vehicular engines operating under lean burn conditions are effective for fuel cost improvement and environmental protection. Under these excess oxygen conditions, however, the NO_x components cannot be efficiently removed by a traditional three-way catalyst, which is effective only under stoichiometric conditions. Developing new technologies to eliminate NO_x emission from lean-burn exhaust has, therefore, attracted much attention in environmental catalysis. One of the most promising technologies is NO_x storage reduction (NSR, also known as lean NO_x trap, LNT), which was first developed by Toyota Corporation in the 1990s.[1–4] Generally, NSR is an inherently transient operation in which the gases fed to the catalysts are periodically switched between fuel-lean and fuel-rich streams. Under lean conditions, NO is oxidized to more active NO_2 followed by storage on the catalyst; under a subsequent fuel-rich atmosphere, the stored NO_x is reduced and thus the active sites are released for the next cycle.[4,5] Storage periods of 1–2 min followed by rich phases of several seconds are typically used in real engines;[3] however, many studies on NSR catalysts have used long rich regeneration periods compared to those of real systems. Consequently, minimizing the duration of the rich phase without decreasing NO_x conversion is highly desired for avoiding excessive fuel consumption. In principle, a NSR catalyst should consist of three major components: (1) noble metals (Pt, Pd), for NO oxidation/reduction; (2) alkali metal or alkaline earth metal compounds (*e.g.* Ba), for NO_x sorption; (3) a high-surface-area support (*e.g.* Al_2O_3).[3,6]

Ceria (CeO_2) has been regarded as one of the most significant components in many catalytic systems due to its unique redox properties and high oxygen storage capacity (OSC), releasing/taking up oxygen through redox processes involving the Ce^{4+}/Ce^{3+} couple.[7] Moreover, several features of CeO_2 appear to be beneficial for NSR reactions: sustaining high metal dispersion, promoting the water-gas shift reaction and steam

State Key Joint Laboratory of Environment Simulation and Pollution Control, Research Center for Eco-Environmental Sciences, Chinese Academy of Sciences, Beijing, 100085, China. E-mail: honghe@rcees.ac.cn

† Electronic supplementary information (ESI) available: TEM and HRTEM images of NSR catalysts, the effect of CO_2 and H_2O on the catalytic performance, NH_3 selectivity, XPS analyses of Pt and Ce, Pt–L_{III} EXAFS, methanol adsorption and H_2-TPR fitting results. See DOI: 10.1039/c5cy01660f

‡ These authors contributed equally to this work.

reforming reaction, and providing surface basicity to benefit the formation of carbonates.[7–9] With these in mind, CeO_2 has been used as either an additive or support, and its role varies according to research focus.[10–21] As for NSR catalysts containing BaO, Casapu *et al.*[22] found that ceria serving as a support significantly improved the NO_x storage capacity (NSC), due to the high instability of $BaCeO_3$ in the presence of NO_2/H_2O or CO_2 at 300–500 °C. Compared with conventional $Pt/BaO/Al_2O_3$ catalysts, a higher NO_x storage capacity and better regeneration behaviour were also observed for $Pt/BaO/CeO_2$ (or $Pt/BaO/CeO_2/Al_2O_3$) at low temperatures by Shi *et al.*,[13] which was attributed to enhanced Pt dispersion and improved redox properties due to ceria introduction (or modification). It has also been found[23] that the addition of CeO_2 to Pt/Al_2O_3 helped maintain metallic Pt dispersion on Al_2O_3 and introduce more NO_x adsorption sites, finally relating to the enhanced NSC. Indeed, the strong metal–support interaction (SMSI) between noble metals and ceria has been recognized as an important factor that affects both the microstructure and redox properties of ceria-based catalysts.[7,24,25]

The design and fabrication of catalytic materials with desired performance are key issues in heterogeneous catalysis. Recently, the structure-sensitive behaviour of nanosized ceria systems has attracted significant attention owing to their unique catalytic properties, and fruitful results have been achieved in catalytic applications such as CO oxidation,[26–28] water-gas shift reaction,[29] CO_2 reforming,[30] NO reduction[31,32] and ethanol reforming.[33] Si *et al.*[29] have found that gold supported on CeO_2 nanorods and nanopolyhedra exhibited higher activity for the water-gas shift reaction than that supported on nanocubes, due to the higher levels of defects in the former two. As for the preferential CO oxidation in H_2-rich gas, Yi *et al.*[34] confirmed that the catalytic activity of Au/CeO_2 catalysts varied as a function of the CeO_2 nanomaterial support as follows: nanorods > nanopolyhedra > nanocubes. More recently, higher activity was achieved for $MnO_x/ZrO_2–CeO_2$ in the selective catalytic reduction of NO by using $ZrO_2–CeO_2$ nanorods as a support compared with that using nanocubes and nanopolyhedra.[31] Further results revealed by XPS, Raman, HRTEM, and kinetic measurements demonstrated that the excellent catalytic activity of the nanorod catalyst could be attributed to adsorbed surface oxygen and oxygen vacancies associated with $ZrO_2–CeO_2$ nanorods' exposed (110) and (100) planes. The achievements mentioned above confirmed that the activity of CeO_2-based catalysts is often shape-dependent, creating a guideline for designing catalysts with high efficiency, and also for revealing the structure–activity relationship.

To the best of our knowledge, however, there has been little information concerning the morphology effect of CeO_2 nanomaterials on the activity of CeO_2-supported NSR catalysts under cyclic lean–rich conditions. To highlight this issue, herein, nanosized ceria with the shapes of rods, cubes, and particles was synthesized and used as a support for $Pt/BaO/CeO_2$ catalysts. Catalytic tests were performed in a transient flow reactor system and a series of characterization techniques including XRD (powder X-ray diffraction), TEM (transmission electron microscopy), XPS (X-ray photoelectron spectra), EXAFS (extended X-ray absorption fine structure), NO_x–TPD (NO_x temperature programmed desorption), H_2-TPR (H_2 temperature programmed reduction) and *in situ* DRIFTS (Diffuse Reflectance Infrared Fourier Transform Spectroscopy) were conducted to investigate the electrical, chemical, and structural properties. Even under harsh lean–rich cycling operation (90 s *vs.* 6 s) and a high GHSV of 360 000 h^{-1}, it was found that superior NO_x storage–reduction performance was achieved on the CeO_2-nanorod supported NSR catalyst, which was attributed to the higher numbers of oxygen vacancies in the exposed (110) and (100) planes of ceria.

Experimental

Catalyst preparation

Preparation of different shaped CeO_2 nanomaterials. The CeO_2 nanorods and nanocubes were prepared by a hydrothermal method modified on the basis of previous studies.[26,30,35] Specifically, 6.9 mmol of cerium nitrate (AR grade, Tianjin Fuchen Chemical Reagent Factory, China) and specific amounts of NaOH (AR grade, Sinopharm Chemical Reagent Beijing Co., Ltd., China, 0.375 mol for nanorods, 0.75 mol for nanocubes) were dissolved in 30 ml and 50 ml of deionized water, respectively. Then the mixture was stirred for 60 min to obtain a purple slurry and subsequently transferred into a Teflon-lined stainless autoclave at a temperature of 100 °C and held for 12 h for nanorods (for nanocubes, this process was performed at 180 °C for 24 h). The fresh precipitates were thoroughly washed with deionized water and anhydrous ethanol (AR grade, Sinopharm Chemical Reagent Beijing Co., Ltd., China) to remove any possible ionic remnants. The solid obtained was dried at 60 °C in air for 24 h and calcined at 550 °C for 4 h in air.

The CeO_2 nanoparticles were prepared *via* a traditional precipitation method: 6.9 mmol of $Ce(NO_3)_3{\cdot}6H_2O$ was dissolved in 30 ml of deionized water, and then 50 ml of 0.01 mol L^{-1} NaOH solution was dropped into the above solution with vigorous stirring. After 60 min of stirring, the mixture was transferred into a water bath kettle at 30 °C for 12 h. The fresh precipitates were washed with deionized water and anhydrous ethanol, dried at 60 °C in air for 24 h and calcined at 550 °C for 4 h in air.

Catalyst preparation. The NSR catalysts were synthesized by an impregnation method using nanosized CeO_2 materials as supports. First, the CeO_2 (nanoparticles, nanocubes, or nanorods) was impregnated in a $Ba(CH_3COO)_2$ (AR grade, Sinopharm Chemical Reagent Beijing Co., Ltd., China) solution. After stirring for 60 min, the excess water was removed in a rotary evaporator at 50 °C. The samples were then dried at 120 °C overnight and calcined at 500 °C for 3 h in air. Subsequently, Pt was loaded on the surface of Ba/CeO_2 by the same procedure using $PtCl_4$ as a precursor. The catalysts

prepared with CeO_2 nanoparticles, nanocubes, and nanorods are hereafter denoted as Pt/BaO/CeO_2-NP, Pt/BaO/CeO_2-NC, and Pt/BaO/CeO_2-NR, respectively, with a nominal Ba loading of 8 wt% and a value of 1 wt% for Pt loading.

Characterization

Powder X-ray diffraction (XRD) patterns were measured on a PANalytical X'Pert PRO X-ray diffractometer (Netherlands, Cu K_α as radiation source, λ = 0.154 nm).

The specific surface areas of the catalysts were obtained at −196 °C over the whole range of relative pressures, using a Quantachrome Quadrasorb SI-MP. Prior to N_2 physisorption, the catalysts were degassed at 300 °C for 5 h. Specific surface areas were calculated from these isotherms by applying the BET equation in the 0.05–0.3 partial pressure range. The component contents of catalysts were analyzed using an inductively coupled plasma instrument (OPTMIA 2000DV) with a radial view of the plasma. All samples were dissolved using a strong acid solution before testing. Transmission electron microscopy (TEM) images with low magnification were obtained on a Hitachi H-7500 transmission electron microscope (Hitachi) with an acceleration voltage of 80 kV. High-resolution transmission electron microscopy (HR-TEM) images were obtained on a JEOL JEM 2010 TEM with 200 kV acceleration voltage. High-angle annular dark-field scanning transmission electron microscopy (HAADF-STEM) and energy dispersive X-ray spectroscopy (EDS) elemental mapping were performed on a probe Cs-corrected JEOL JEM-ARM 200 F operated at 200 kV.

X-ray photoelectron spectra (XPS) measurements were recorded in a scanning X-ray microprobe (PHI Quantera, ULVAC-PHI, Inc.) using Al K_α radiation. Binding energies were calibrated using the C 1 s peak (BE = 284.8 eV) as standard.

Extended X-ray absorption fine structure (EXAFS) measurements were carried out on the XAFS station in 1W1B beamline of Beijing Synchrotron Radiation Facility (BSRF) operating at about 150 mA and 2.2 GeV. Data were analyzed using the program REX2000 (Rigaku Co.). The EXAFS oscillation $\chi(k)$ was extracted using spline smoothing with a Cook–Sayers criterion,[36] and the filtered k^3-weighted $\chi(k)$ was Fourier transformed into R space (k range: 3–12 $Å^{-1}$ for Pt-L_{III} EXAFS). In the curve fitting step of Pt-L_{III} EXAFS, the backscattering amplitude and phase shift were calculated using FEFF8.4.[37]

NO_x temperature programmed desorption (NO_x-TPD) experiments were performed in a Micromeritics AutoChem II 2920 apparatus, equipped with a computer-controlled CryoCooler, a thermal conductivity detector (TCD), and a quadrupole mass spectrometer (MKS Cirrus). The samples were first pre-reduced with 10% H_2/Ar at 450 °C for 30 min, and cooled down to room temperature. After purging with He for 30 min, the gas was switched to NO_2 adsorption for 60 min. After He flow for another 30 min, the temperature was increased to 900 °C at a heating rate of 10 °C min^{-1}, and the signal of NO (m/z = 30) was recorded simultaneously. To avoid the influence of H_2O, a cold trap was set before the MS detector.

H_2 temperature programmed reduction (H_2-TPR) was performed in the same instrument as the NO_x-TPD. The 100 mg samples were pretreated at 450 °C in a flow of air (50 mL min^{-1}) for 30 min and cooled down to room temperature. Then reduction profiles were obtained by passing a flow of 10% H_2/Ar through the sample at a rate of 50 mL min^{-1}, during which the temperature was increased from 50 to 950 °C at a ramp rate of 10 °C min^{-1}.

In situ DRIFTS experiments were performed on an FTIR spectrometer (Nicolet Nexus 670) equipped with a smart collector and an MCT/A detector cooled with liquid nitrogen. Prior to each experiment, the sample was pretreated with 3% H_2/N_2 at 450 °C for 1 h, and then cooled down to the specified temperature. A mixture containing 500 ppm NO and 8% O_2 at a total flow rate of 300 mL min^{-1} was employed to investigate the behavior of the NSR catalyst for NO_x storage, while a stream of 3% H_2 was used to measure the activity of ad-NO_x over the Pt/Ba/CeO_2 catalyst. All spectra presented here were recorded by accumulating 30 scans with a resolution of 4 cm^{-1}.

Catalytic activity measurements

NO_x storage capacity experiment. NO_x uptake experiments were carried out under fuel-lean conditions as a function of temperature. Before each experiment, the catalyst was pretreated in 3% H_2/N_2 for 1 h at 450 °C, and then cooled to the desired temperature. A mixture of 500 ppm NO, 8% O_2, 1% CO_2 (if used), and 2% H_2O (if used) at a total flow rate of 300 mL min^{-1} was used to simulate the fuel-lean exhaust, using N_2 as a balance gas. The outlet NO_x (NO + NO_2) concentration was monitored by a chemiluminescence detector (ECO Physics CLD 62). The outlet NH_3 was analyzed using a chemiluminescence detector (ECO Physics CLD 822).

Cyclic NO_x storage reduction tests. NSR cyclic measurements were conducted with 100 mg of catalyst using a fixed-bed quartz reactor. The reactor was connected to a pneumatically actuated four-way valve, which provides quick switching between the lean and rich atmospheres. Constant flows (300 mL min^{-1}) of 500 ppm NO + 8% O_2 + 1% CO_2 (if used) + 2% H_2O (if used) and 500 ppm NO + 3% H_2 + 1% CO_2 (if used) + 2% H_2O (if used) were introduced alternately, during which a lean period of 90 s and a rich period of 6 s were performed between 200 °C and 400 °C. The NO_x conversion was averaged over 20 lean/rich cycles to give a mean value according to the following formula:

$$NO_x \text{ conversion}(\%) = \frac{NO_{x,in} - NO_{x,out}}{NO_{x,in}} \times 100\%.$$

The NH_3 selectivity was calculated by the following formula:

$$NH_3 \text{ selectivity} = \frac{NH_{3,out}}{NO_{x,in} - NO_{x,out}} \times 100\%.$$

Results and discussion

Structural features of nanoceria and Pt/BaO/CeO_2 catalysts

The morphology of CeO_2 nanomaterials and corresponding NSR catalysts was characterized by TEM and HRTEM (Fig. 1 and S1†). As shown in Fig. S1a,† the CeO_2 nanoparticles (denoted as CeO_2-NP hereafter) displayed a mean diameter of around 9 nm. HRTEM images (Fig. 1a) further revealed that the CeO_2-NP were dominated by (111) planes together with small amounts of (100) planes, exhibiting interplanar spacings of 0.31 and 0.27 nm, respectively. This feature indicates that CeO_2 nanoparticles were in the form of a truncated octahedron enclosed by eight (111) and six (100) planes, with the structural model presented in the insert of Fig. 1a.[38,39] As shown in Fig. S1b,† the CeO_2 nanocubes (CeO_2-NC), with an inhomogeneous grain size ranging from 10–50 nm, were mostly well-developed. Calculating for 200 nanocubes from the HRTEM images, the average size of *ca.* 0.27 nm was obtained. An interplanar spacing of 0.27 nm implies that the CeO_2 nanocubes are enclosed by six polar (100) planes, showing a cubic structure (Fig. 1b). The CeO_2 nanorods (CeO_2-NR) had a mean diameter of 8.1 nm and a length from 40–110 nm (Fig. S1c†). Fig. 1c–d depicts the HRTEM image of CeO_2-NR combined with a fast Fourier transform (FFT) analysis. According to the FFT analysis, three kinds of lattice fringe directions attributed to (111), (002), and (220) were observed for the nanorods, which have respective interplanar spacings of 0.31, 0.27, and 0.19 nm in the HRTEM image. The nanorods show a 1D growth structure with a preferred growth direction along [110], and are enclosed by (110) and (100) planes.

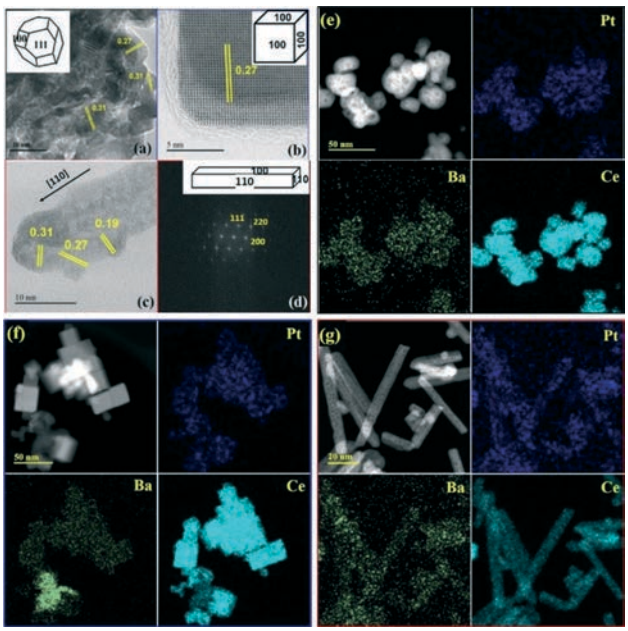

Fig. 1 HRTEM images of CeO_2-NP (a), CeO_2-NC (b), and CeO_2-NR (c), FFT analysis of (c) (d); HAADF-STEM EDS elemental mapping images of Pt/BaO/CeO_2-NP (e), Pt/BaO/CeO_2-NC (f), and Pt/BaO/CeO_2-NR (g).

After the deposition of Ba and Pt, it can be clearly seen from Fig. S1d–f† that the three different CeO_2 nanomaterials maintained their original crystal shapes, while no structural features of Pt and Ba can be observed. With this in mind, elemental maps were measured by high-angle annular dark-field scanning transmission electron microscopy (HAADF-STEM) (Fig. 1e–g), revealing that the active components of Pt and Ba were highly dispersed on all three NSR catalysts.

The specific surface areas of CeO_2 nanomaterials and corresponding NSR catalysts are listed in Table 1. Pure CeO_2 nanoparticles had the largest surface area (134.9 $m^2\ g^{-1}$), while the CeO_2 nanocubes gave the lowest value of 26.5 $m^2\ g^{-1}$. After deposition of Pt and BaO, the surface areas of Pt/BaO/CeO_2-NP, Pt/BaO/CeO_2-NR, and Pt/BaO/CeO_2-NC decreased to 115.7, 84.2, and 20.0 $m^2\ g^{-1}$, respectively. The ICP-OES data (Table 1) showed that the contents of the active components had no significant difference among the NSR catalysts, all of which were close to the nominal values (1% Pt and 8% BaO).

The crystal structures of the different shaped samples were investigated by XRD and shown in Fig. 2. The diffraction peaks at 28.5, 33.0, 47.5, 56.3, 59.1, 69.4, 76.7, 79.1 and 88.4° could be ascribed to the fluorite structure of ceria (JCPDS no. 43-1002), while no peaks from Pt species were observed in any of the samples, indicating high dispersion and further confirming the results of the elemental maps. Using the Scherrer equation for the peak due to the (111) plane, the CeO_2 sizes of CeO_2 nanomaterials and corresponding NSR catalysts were calculated (Table 1), giving values in good agreement with the results of the HRTEM. In every Ba-containing sample, XRD analysis confirmed the decomposition of $Ba(CH_3COO)_2$ into crystalline $BaCO_3$ (JCPDS no. 44-1487) during catalyst calcination, in agreement with previous results.[13]

Catalytic performance

NO_x storage performance. The NO_x breakthrough curves *versus* time of Pt/BaO/CeO_2-NP, Pt/BaO/CeO_2-NC and Pt/BaO/CeO_2-NR at different temperatures are recorded as shown in Fig. S2.† As soon as the lean feed was switched from the bypass loop to the catalysts, the NO_x concentration in the outlet dropped sharply from 500 ppm to 0 ppm, followed by a complete uptake process. With increasing time, the outlet NO_x concentration gradually increased and a saturation state was achieved slowly by the end of 3600 s. The areas between the inlet feed and the breakthrough curves represent the NO_x storage capacities (NSC), which were calculated and summarized in Fig. 3. It was apparent that Pt/BaO/CeO_2-NR showed much larger NSC than Pt/BaO/CeO_2-NP and Pt/BaO/CeO_2-NC at all temperatures tested. Specifically, Pt/BaO/CeO_2-NR presented the highest NO_x storage capacity at 350 °C, affording about 913.8 μmol g_{cat}^{-1}, which approached the theoretical NO_x storage capacity (937.4 μmol g_{cat}^{-1}, see the ESI†).

The oxidation of NO to NO_2 is regarded as a key step in the NO trapping process, during which platinum plays a

Table 1 Specific surface area, active component loading, and particle size (D) of CeO_2 nanomaterials and Pt/BaO/CeO_2 samples

Catalyst	Surface area ($m^2\ g^{-1}$)	Pt loading (%)	BaO loading (%)	D^a (nm)	CeO_2 size^b (nm)
CeO_2-NP	134.9	—	—	—	11.2
Pt/BaO/CeO_2-NP	115.7	1.07	7.50	8.8 ± 2.4	11.3
CeO_2-NC	26.5	—	—	—	33.3
Pt/BaO/CeO_2-NC	20.0	0.92	7.33	26.9 ± 13.7	33.1
CeO_2-NR	103.6	—	—	—	12.3
Pt/BaO/CeO_2-NR	84.2	1.01	7.82	(8.1 ± 1.4) × (40–110)	12.2

^{a} Caculated for 200 CeO_2 nanomaterials from the HRTEM images. ^{b} Caculated based on the CeO_2 diffraction peak at 2θ = 28.5° by applying the Scherrer equation.

significant role.[40–42] Fig. S3† compares the molecular ratio of $NO_2/(NO + NO_2)$ over the series of Pt/BaO/CeO_2 catalysts at the end of the storage process, where the NO_2/NO_x ratio reached a steady state. For a given NSR catalyst, a gradually increased $NO_2/(NO + NO_2)$ always relates to an increase in the NSC value within the temperature range of 200–350 °C, confirming the key role of NO oxidation.

The effects of CO_2 and H_2O on the NO_x storage process were investigated over all the NSR catalysts, with the results shown in Fig. S4.† Introducing of 1% CO_2 and 2% H_2O into the feed gas decreased the NO_x storage capacity, while the extent of NSC reduction was quite different among the tested NSR samples. Over Pt/BaO/CeO_2-NP and Pt/BaO/CeO_2-NC, drastic decreases in NSC values were observed within the whole temperature range if compared with those in the absence of H_2O and CO_2. In the presence of H_2O and CO_2, in contrast, Pt/BaO/CeO_2-NR still presented a relatively high NO_x storage capacity. At the temperature of 350 °C, Pt/BaO/CeO_2-NR afforded about 713.6 μmol NO g_{cat}^{-1}, which is nearly 80% of that without H_2O and CO_2.

Dynamic NO_x storage and reduction performance. The NO_x removal efficiency is not only concerned with the storage capacity in the lean phase, but also related to the reduction of trapped NO_x during the rich phase. Minimizing the duration of the rich phase can improve the fuel efficiency, so a rich regeneration time of several seconds is typically used in real systems.[33] However, many studies use a longer rich period compared to those of real engines. In this study, the NO_x removal efficiency was investigated under harsh cycling conditions, with a lean period of 90 s and a rich period of 6 s at a quite high gas hourly space velocity (GHSV) of 360 000 h^{-1}.

Fig. 4a–c depicts the evolution of NO_x in the outlet feed over twenty lean/rich cycles for all NSR catalysts at temperatures between 200 and 400 °C. The averaged twenty-cycle NO_x conversion values over Pt/BaO/CeO_2-NP, Pt/BaO/CeO_2-NC and Pt/BaO/CeO_2-NR are compared in Fig. 4d. On Pt/BaO/CeO_2-NR, it was easy to see that the outlet NO_x breakthrough was close to 0 ppm during all the cycles performed at 200 °C and 400 °C. At other temperatures, NO_x spilled out still maintained relatively low values (10–60 ppm) at the end of the lean durations. This indicates that Pt/BaO/CeO_2-NR possessed the highest catalytic performance, obtaining nearly 100% NO_x conversion from 200 °C to 400 °C. Similarly, the NO_x removal efficiency of Pt/BaO/CeO_2-NP was quite high, reaching 93.5% at all temperatures. For the Pt/BaO/CeO_2-NC catalyst, however, the outlet NO_x breakthrough increased significantly (to 100 ppm at 200 °C) during the first cycle. And even worse, much more NO_x spilled out and reached around 400 ppm after 5 cycles, presenting extremely low NO_x removal.

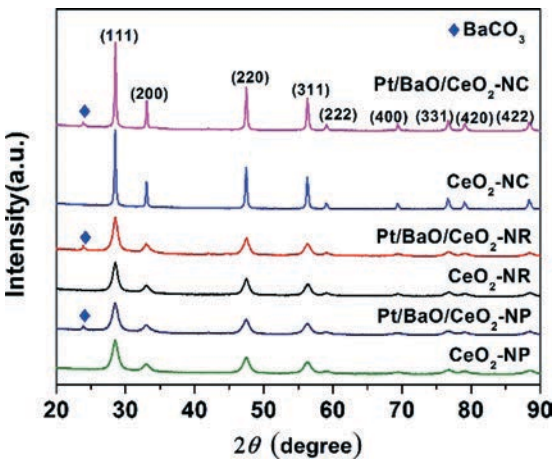

Fig. 2 XRD patterns of CeO_2 nanomaterials and Pt/BaO/CeO_2 samples.

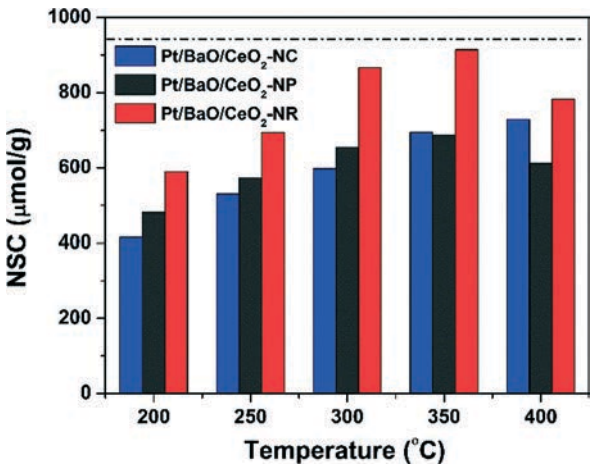

Fig. 3 NO_x storage capacities (NSC) tested at different temperatures over Pt/BaO/CeO_2 catalysts.

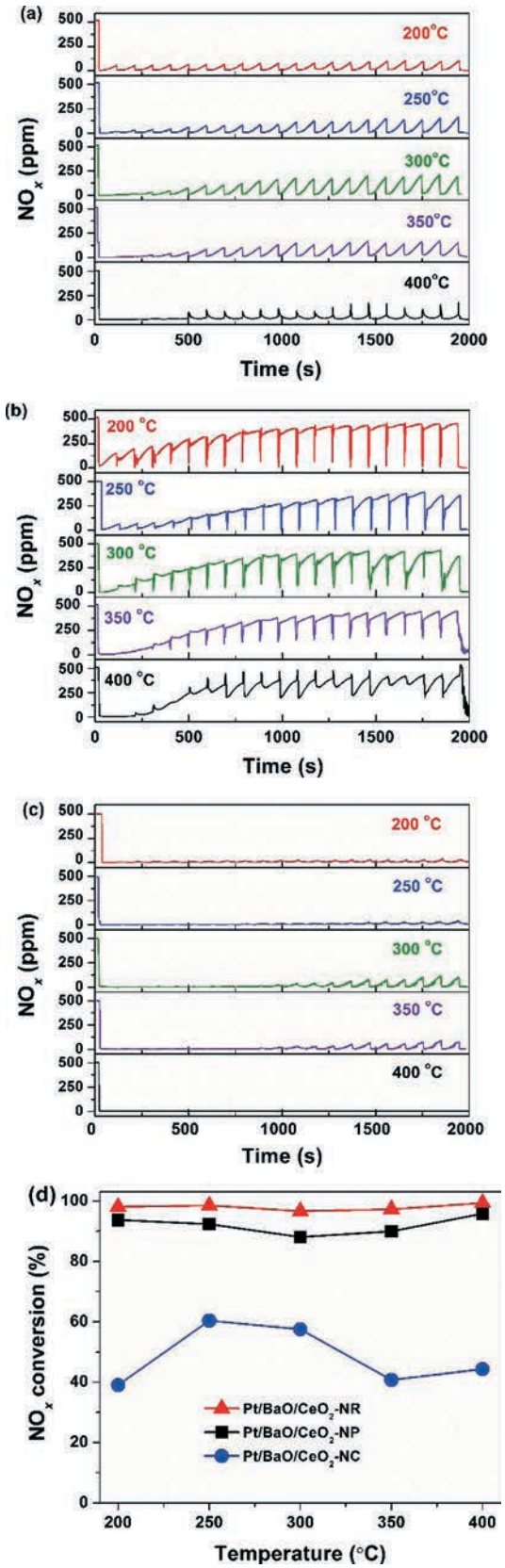

Fig. 4 Evolutions of NO_x concentrations under cyclic lean–rich conditions at different temperatures on Pt/BaO/CeO_2-NP (a), Pt/BaO/CeO_2-NC (b), and Pt/BaO/CeO_2-NR (c); average NO_x conversion over all NSR catalysts under cyclic lean–rich conditions at different temperatures (d).

Ammonia, as the main by-product of the NSR process, was also measured under cyclic lean–rich conditions, with the results shown in Fig. S5 and Table S1.† Obviously, the three NSR catalysts show quite different features of NH_3 release. Over Pt/BaO/CeO_2-NP, the selectivity to NH_3 decreased monotonically with a rise in temperature, changing from 52.8% at 200 °C to 0.88% at 400 °C. In the whole temperature range, Pt/BaO/CeO_2-NC exhibited much higher production of NH_3 than Pt/BaO/CeO_2-NP, particularly at temperatures above 250 °C. Among the tested NSR catalysts, interestingly, Pt/BaO/CeO_2-NR shows the lowest NH_3 selectivity, exhibiting the lowest value of 0.74% at 300 °C and the highest one of 11.54% at 200 °C.

In the initial 2 lean/rich cycles (Fig. 4b), it is clear that the NO_x conversion over Pt/BaO/CeO_2-NC was well related to the NSC value. As cycles continued, however, the NO_x was not fully trapped under lean conditions, and was not further reduced during the rich phase. Such gradual deactivation with time on stream was more pronounced within the temperature range of 300–400 °C (Fig. 4b), which was also indicated by the average NO_x conversion over 20 lean/rich cycles (Fig. 4d). This result indicates that, in our case, the NO_x removal efficiency under a large scale is not only concerned with the storage capacity under lean conditions, but also related to the reduction efficiency for the trapped NO_x during the rich phase. Under rich conditions, the consumption of H_2 was involved in the reduction of released NO_x and residual oxygen species on the catalyst surface. Because of a long lean period (90 s) and a short rich period (6 s), the residual oxygen on the surface would increase gradually with an increase in cyclic operation, reducing of which needs a greater amount of H_2 if compared with the initial several cycles.[43] As a result, the amount of H_2 for the reduction of trapped NO_x decreased with time going on, leading to the partial regeneration of the storage sites in the rich phase and a decrease in NO_x storage under lean conditions. A slightly decrease in NO_x conversion was also observed on Pt/BaO/CeO_2-NR and Pt/BaO/CeO_2-NP during the lean–rich cycling operation, particularly at the temperature of 300 °C (Fig. 4). A further intensive study will be performed to reveal the temperature and sample shape dependency of the NO_x conversion over Pt/BaO/CeO_2.

The formation of ammonia and its reaction pathway for the NSR process have been intensively investigated by Courtois and co-workers.[16,44] Over Pt/BaO/Al_2O_3, it was proposed that the NH_3 formation rate *via* NO_x reduction by H_2, is higher that the NH_3 reaction rate with NO_x to form N_2, leading to NH_3 emission during the NSR process when H_2 is employed as a reductant.[44] When Pt/BaO/Al_2O_3 is modified with an optimal amount of Ce, interestingly, the ammonia selectivity significantly decreased, attributed to the promotion of ammonia oxidation into N_2 *via* the available oxygen at the catalyst surface.[16] Among the three NSR catalysts, in our case, Ce XPS and H_2-TPR results (in the following section) indicated that the greatest amount of surface active oxygen trapped by oxygen vacancies was available from Pt/BaO/CeO_2-

NR. Such active oxygen from ceria possibly enhances the ammonia oxidation to produce N_2. As a consequence, a low NH_3 selectivity was achieved on Pt/BaO/CeO_2-NR due to the high amount of active oxygen trapped by oxygen vacancies, in accordance with the results of previous studies.[16,44]

The influences of CO_2 and H_2O on the NSR performance under lean–rich cycling operation were also evaluated, with the results shown in Fig. S6.† Similar to the NO_x storage process, an inhibition effect of H_2O and CO_2 on NO_x conversion was also observed over all the samples. Among the tested NSR catalysts, Pt/BaO/CeO_2-NR showed the highest NO_x removal efficiency, exceeding 80% in the temperature range of 200–350 °C.

Thermal stabilities of the stored NO_x

The NO_x storage features and thermal stabilities of the NO_x stored on Pt/BaO/CeO_2-NP, Pt/BaO/CeO_2-NC and Pt/BaO/CeO_2-NR were compared by TPD experiments after NO_2 adsorption at room temperature (Fig. 5). Because NO_2 is easily dissociated to the NO ionization fragment under our MS conditions, the signal of NO_2 (m/z = 46) in our experiment was very weak and the main signal was NO (m/z = 30).[43] Clearly, Pt/BaO/CeO_2-NR showed the largest amount of desorbed NO, while the amount of desorbed NO of Pt/BaO/CeO_2-NP was approximately the same as that of Pt/BaO/CeO_2-NC. This was consistent with the NO_x storage capacity as presented in Fig. 3. It is noteworthy that Pt/BaO/CeO_2-NC exhibits the lowest amount of desorbed NO at temperatures below 350 °C, while the strongest peak is centered at much higher temperature than for the other two catalysts. This result clearly shows that the ad-NO_x on Pt/BaO/CeO_2-NC possesses high stability, benefiting for NO storage at high temperatures. As a result, a larger NSC value was obtained over this catalyst at a temperature of 400 °C (Fig. 3). On the other hand, the ad-NO_x with high stability makes against its release under fuel-rich conditions, thus lowering NO_x conversion over Pt/BaO/CeO_2-NC (Fig. 4).

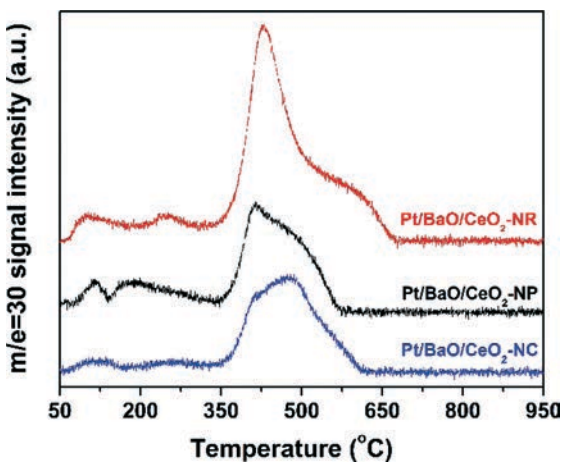

Fig. 5 NO_x-TPD profiles of the NSR catalysts.

Chemical states and oxygen vacancies

XPS analysis was performed to verify the state of Pt and Ce on the surface of the NSR catalysts. Fig. S7† shows the Pt 4f XPS spectra of fresh Pt/BaO/CeO_2 catalysts, and those reduced by H_2 (hereafter denoted as Pt/BaO/CeO_2-R), considering that the samples were pre-treated by H_2 before activity measurement. The binding energies of the individual peaks of the Pt 4f spectra are summarized in Table S2.† According to previous studies,[45,46] the peaks at 72.5 (4f7/2) and 75.8 eV (4f5/2) should belong to PtO while those at 74.1 (4f7/2) and 77.5 eV (4f5/2) can be attributed to PtO_2. It could be concluded that platinum on all the three NSR catalysts was present in the form of PtO and PtO_2. In addition to the peaks belonging to PtO and PtO_2, the H_2-treated NSR catalysts also showed peaks at 71.0 (4f7/2) and 74.2 eV (4f5/2) corresponding to Pt^0. Thus the reduced NSR catalysts contained metallic Pt and Pt oxides.

The EXAFS of Pt-L_{III} edges were also measured over all the samples (Fig. S8†). The results of curve-fitting analysis of the EXAFS are summarized in Table S3.† In the Fourier transform spectrum of Pt foil, the peak at 2.77 Å is assigned to the Pt–Pt bond. As for the reference sample of PtO_2, the peaks at 2.02 and 3.10 Å are assigned to the Pt–O and Pt–O–Pt bonds, respectively. Interestingly, only the intense peak at 2.00 Å corresponding to the Pt–O bond was observed over the fresh NSR catalysts. The formation of defined Pt–O–Ce bonds, as reported in the references,[47,48] which may inhibit the sintering of Pt could not be observed in our Pt/BaO/CeO_2 catalysts, in agreement with previous studies.[49,50] Moreover, Pt–Pt or Pt–O–Pt peaks could not be observed in all the NSR catalysts, suggesting that there are no large Pt metal or oxide particles. In other words, highly dispersed Pt oxides were present on the surface of the CeO_2 supports, in agreement with the elemental mapping images. Generally, Pt^0 is considered to be the active site for the catalytic reaction. Therefore, the EXAFS of Pt-L_{III} edges over the reduced NSR catalysts were also presented. After H_2 reduction at 450 °C, the Pt–O peak decreased significantly compared with the fresh catalysts. In addition, the Pt–Pt peak could be observed in the reduced catalysts. These results suggested that all of the Pt species were reduced from Pt^{4+} to Pt^0 and Pt^{2+}, further confirming the XPS results.

Fig. 6a–c shows the Ce 3d XPS spectra of the pure CeO_2 nanomaterials and the NSR catalysts, together with the corresponding peak fitting results. The v′, and u′ peaks correspond to Ce^{3+}; while v, v″, v‴, u, u″, and u‴ are contributed by Ce^{4+}.[51–53] The peak positions for all the samples are listed in Table S4.† The Ce^{3+} concentration in the CeO_2 nanomaterials and corresponding NSR catalysts was calculated by analysis of the integrated peak area, with the equation shown as follows:

$$\left[Ce^{3+}\right] = \frac{A_{v'} + A_{u'}}{A_{v'} + A_{u'} + A_{v'} + A_{v''} + A_{v'''} + A_{u} + A_{u''} + A_{u'''}},$$

where A_i is the integrated area of peak "i".

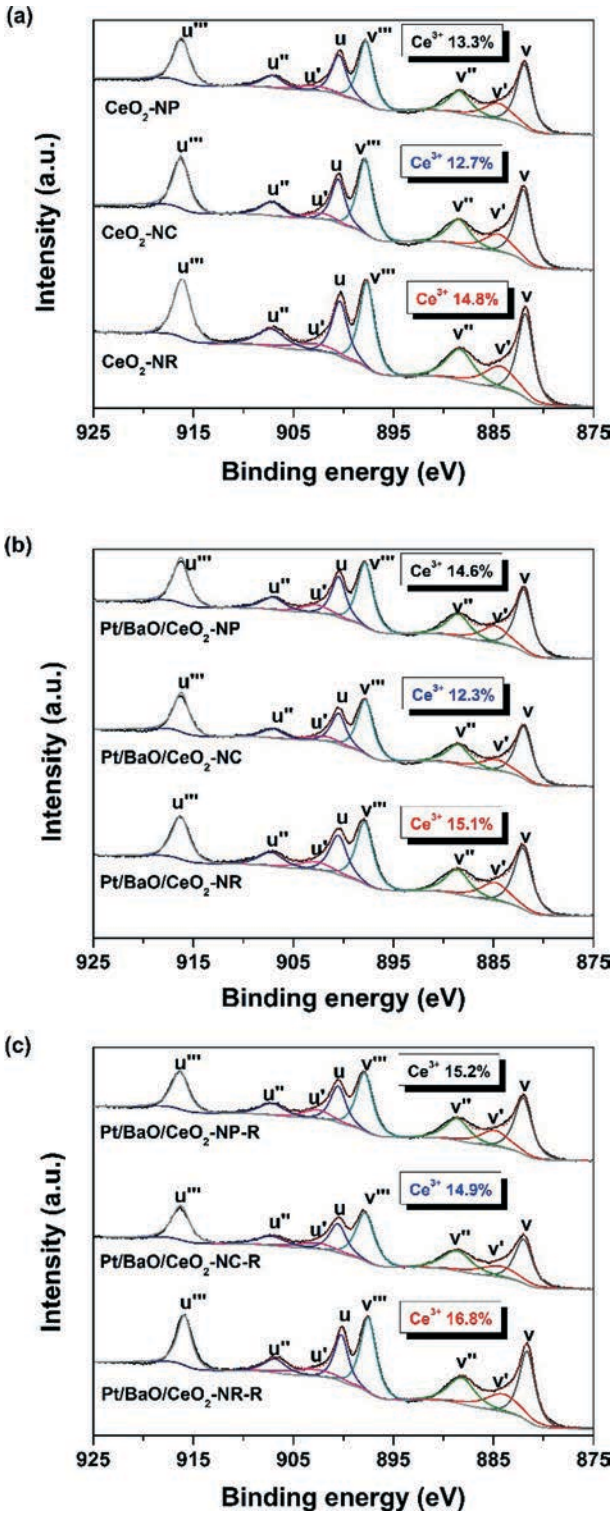

Fig. 6 Ce 3d XPS spectra of three different shaped CeO_2 (a), Pt/BaO/CeO_2 (b), and Pt/BaO/CeO_2-R (c).

As we all know, once Ce^{3+} appears in fluorite-structure ceria, oxygen vacancies will be produced by the transformation of Ce^{4+} to Ce^{3+}, $4Ce^{4+} + O^{2-} \rightarrow 2Ce^{4+} + 2Ce^{3+} + \square + 0.5O_2$ (where $\square$ presents an empty position).[54] The higher the Ce^{3+} concentration in these materials is, the more oxygen vacancies are formed. Fig. 6 summarizes the concentrations of Ce^{3+} present in the CeO_2 nanomaterials and corresponding NSR catalysts. The results showed that the concentration of oxygen vacancies in the CeO_2 nanorods was much higher than that in the other two CeO_2 nanomaterials. The addition of Ba and Pt components increased the Ce^{3+} contribution on the NSR catalysts, except for Pt/BaO/CeO_2-NC. A similar result was also observed over Ag/CeO_2 by Chang *et al.*, in which the Ag–CeO_2 interaction affected the concentration and structure of oxygen vacancies in the CeO_2 support.[55]

As reported in the literature,[56] the presence of Ce^{4+} can be estimated by the high binding energy band u‴. The proportions of the relative intensity of the u‴ peak over all the samples are shown in Table S4.† The H_2 treatment decreased the proportion of Ce^{4+}, indicating the decrease in the surface content of Ce^{4+}. In other words, the reduced NSR catalysts had a higher amount of Ce^{3+}. Moreover, the proportions of the relative intensity of the u‴ peak on the reduced Pt/BaO/CeO_2-NP, Pt/BaO/CeO_2-NC, and Pt/BaO/CeO_2-NR were 13.4%, 14.3%, and 12.7%, respectively, indicating that the surface content of Ce^{4+} on Pt/BaO/CeO_2-NR was the lowest, in agreement with the concentrations of Ce^{3+}.

Among all the NSR catalysts, the amount of Ce^{3+} in the nanorod-based sample was the highest, which indicates a strong interaction between active components and CeO_2-NR. XPS measurements were also carried out to identify the surface concentrations of Ce^{3+} on the reduced catalysts. As shown in Fig. 6, the surface concentrations of Ce^{3+} as percent of the total Ce on the reduced Pt/BaO/CeO_2-NP, Pt/BaO/CeO_2-NC, and Pt/BaO/CeO_2-NR were 15.2, 14.9, and 16.8%, respectively, indicating that higher concentrations of oxygen vacancies were created by H_2 pre-treatment. Theoretical calculation predicted that[57] the formation of oxygen vacancies on the CeO_2 (110) plane is much more favourable than those on the (100) and (111) planes. As shown in Fig. 1, the CeO_2 nanorods were enclosed by the (110) and (100) facets, while the nanoparticles and nanocubes mainly exposed {(100) + (111)} and (100), respectively. As a result, it is reasonable that the Pt/BaO/CeO_2-NR catalyst exhibits a higher concentration of oxygen vacancies than the other two.

As reported by Lavalley *et al.*,[58] methanol adsorbed on the surface of CeO_2 prefers to dissociate into methoxy species and H^+. In that case, the methoxy species adsorbed on the potential redox sites of CeO_2 exhibits the feature band around 970–1085 cm^{-1}. As a result, the methanol adsorption technique provides a useful method for revealing the amount or states of oxygen vacancies.[59] With this in mind, the IR spectra of Pt/BaO/CeO_2-R (H_2 pretreatment) were recorded during flowing methanol (Fig. S9†).

Within the region of ν(C–O), four bands grow conjointly at 1006, 1032, 1052, and 1114 cm^{-1} during the introduction of methanol, assignable to on-top methoxy (1006 cm^{-1}), bridging methoxy (1032 and 1052 cm^{-1}), and three-coordinate methoxy (1114 cm^{-1}), respectively.[60] After exposure of methanol for 30 min, the intensity of methoxy species was stable for all the samples. Based on the spectra at 30 min, the

amount of redox sites on Pt/BaO/CeO_2-R was calculated from the integral area of 970–1085 cm^{-1} per gram of catalyst, and the results are shown in Table S5.† Obviously, the integral area relating to the redox sites on Pt/BaO/CeO_2-NR was much higher than the other two, indicating a higher concentration of oxygen vacancies, and further confirming the results of Ce 3d XPS.

Redox properties

Fig. S10† shows the H_2-TPR profiles of pure nano-CeO_2 with different shapes. All the CeO_2 samples exhibited a broad reduction peak at 200–500 °C and a high-temperature reduction peak above 600 °C, attributed to surface and bulk ceria reduction, respectively.[7] Fig. 7 illustrates the H_2-TPR profiles and corresponding fitting results of the NSR catalysts with different shaped CeO_2 serving as supports. The peak at temperatures below 300 °C can be assigned to the combined reduction of PtO_x and its neighbouring surface ceria. This surface ceria (denoted as promoted surface ceria hereafter) was intimately in contact with PtO_x, the reduction of which was attributable to the abstraction of O^{2-} by hydrogen and facilitated by the presence of platinum.[61,62] Another peak was observed at an intermediate temperature (*ca.* 570 °C), resulting from the reduction of surface ceria that was more remote from the platinum. In other words, the peak at the intermediate temperature originates from O^{2-} abstraction from surface ceria that is not in direct contact with Pt. Finally, a high-temperature peak was observed at *ca.* 750 °C, due to the reduction of bulk ceria to Ce^{3+}.[61,62] If compared with the pure nano-CeO_2, the reduction of surface ceria occurs at a much lower temperature after loading of Pt and BaO, but the peak intensity significantly changed depending on the shape of CeO_2. This indicates that the morphology of nanoscale ceria has a great influence on the synergistic interaction between platinum and ceria nanostructures (possibly *via* H_2 spillover).

During the H_2-TPR experiments, the total H_2 consumption was measured, with a value of 110.8 μmol for Pt/BaO/CeO_2-NP, 123.6 μmol for Pt/BaO/CeO_2-NC, and 158.8 μmol for Pt/BaO/CeO_2-NR. Based on the fitting results of the H_2-TPR, the H_2 consumption due to the reduction of the total surface ceria for all three NSR catalysts is given in Table S6 (ESI†). The proportions of promoted surface ceria were calculated (the area under the relevant TPR curve divided by the area under all the surface-related curves), giving 13% for Pt/BaO/CeO_2-NP, 3.3% for Pt/BaO/CeO_2-NC and 14.5% for Pt/BaO/CeO_2-NR. This demonstrates that the interaction between platinum and CeO_2-NR is stronger than that with CeO_2-NP and CeO_2-NC. The morphology of nanoscale ceria, therefore, influences the synergistic interaction between platinum and ceria nanostructures. It is worth noting that a sharp peak due to PtO_x reduction was observed for all the NSR catalysts, showing the good dispersion of PtO_x and further confirming the results of elemental maps. The proportions of PtO_x reduction were also calculated, with a value of 13.7% for Pt/BaO/

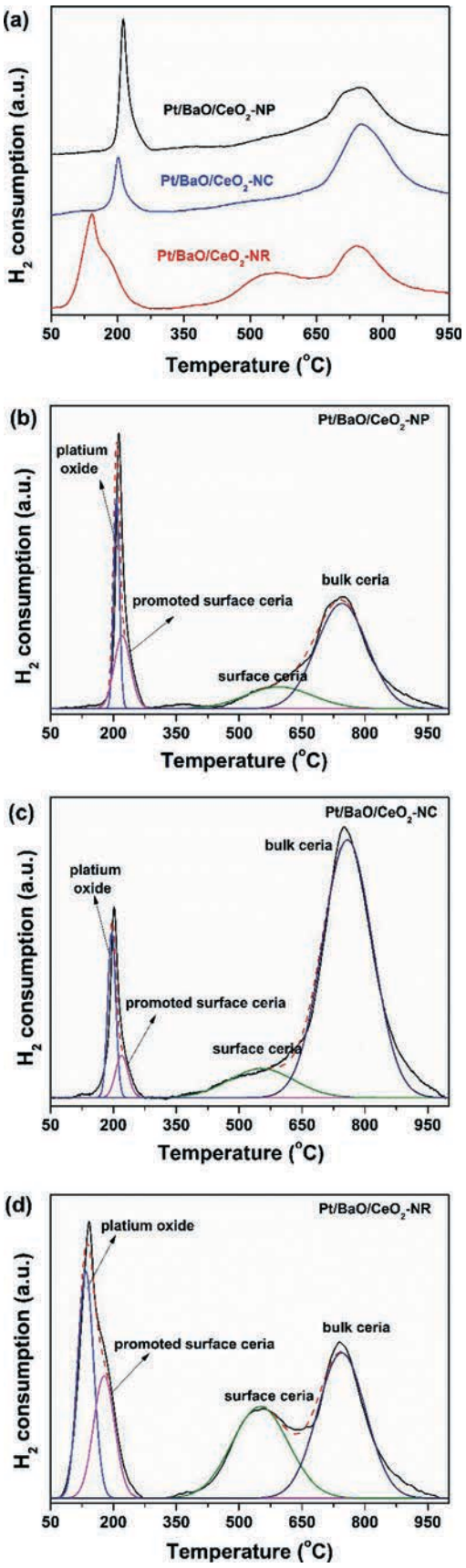

Fig. 7 H_2-TPR profiles of the NSR catalysts based on the different shaped CeO_2 (a), and fitting results for nanoparticle (b), nanocube (c), and nanorod (d) based catalysts, respectively.

CeO_2-NP, 8.2% for Pt/BaO/CeO_2-NC, and 20.0% for Pt/BaO/CeO_2-NR (Table S6†). Over the nanorod-supported sample, meanwhile, the reduction of PtO_x occurred at 137 °C, 76 °C lower than that of Pt/BaO/CeO_2-NP. This result reveals that more Pt species are available on the surface of Pt/BaO/CeO_2-NR, which also exhibits a higher reducibility. As a result, it is reasonable that Pt/BaO/CeO_2-NR is more active for NO oxidation than the other two NSR catalysts (Fig. S3†).

As suggested by Fridell and co-workers,[63] the adsorption of NO_2 and its further transformation into surface nitrates involve the oxidation of the surface or oxygen species by NO_2 to produce NO. It means that, in turn, the reducibility of the NSR catalysts or the availability of active oxygen species plays a crucial role in NO_2 adsorption and storage. Over the Pt/BaO/CeO_2 catalysts presented here, these properties were closely related to the oxygen vacancies on the ceria surface as confirmed by Fig. 6 and 7. Pt/BaO/CeO_2-NP and Pt/BaO/CeO_2-NC exhibit a similar concentration of oxygen vacancies (15.2% for Pt/BaO/CeO_2-NP and 14.9% for Pt/BaO/CeO_2-NC), thus giving a similar amount of desorbed NO in TPD (Fig. 5).

Reaction sites and reaction testing by *in situ* DRIFTS

In Fig. 8, *in situ* DRIFTS show the evolution of surface species during the NO_x storage and reduction process at 350 °C. After exposing the Pt/BaO/CeO_2-NP catalyst to a $NO/O_2/N_2$ mixture for 40 s (Fig. 8a), two bands were observed at 1020 and 1294 cm^{-1}, which were assigned to the symmetric and asymmetric stretching modes of $-NO_2$ due to bidentate nitrate species adsorbed on Ba sites.[10] Meanwhile, another significant band attributed to monodentate nitrate on ceria was observed at 1538 cm^{-1}.[23] With increasing exposure time, bands at 816 and 1770 cm^{-1} appeared and their intensities gradually increased, indicating the formation of bulk nitrate associated with Ba.[64,65] Along with the formation of nitrates, two negative bands appeared at 863 and 1750 cm^{-1}, originating from the decomposition of surface barium carbonate.[23] As time passed, a shoulder was observed at 1349 cm^{-1} which was assigned to free nitrate ions.[66] When the gas feed was switched to a rich atmosphere (Fig. 8b), the bands at 1538, 1349, 1294, and 1020 cm^{-1} disappeared in the first 20 seconds, indicating the high activity of surface nitrates and nitrate ions. In contrast, the bands at 1770 and 816 cm^{-1} decreased gradually, disappearing after 5 min of reduction, suggesting that the bulk nitrates are not as active as those adsorbed on the surface.

The same experiments were carried out on Pt/BaO/CeO_2-NC, with the corresponding DRIFT spectra shown in Fig. 8c and d. The NO_x storage process on Pt/BaO/CeO_2-NC was similar to that on Pt/BaO/CeO_2-NP, except that the intensity of the peak assignable to nitrate ions (1349 cm^{-1}) was much stronger than that on the nanoparticle supported catalyst. Under rich conditions, the nitrates adsorbed on Pt/BaO/CeO_2-NC displayed a significantly lower activity for reaction with H_2, compared with that on Pt/BaO/CeO_2-NP. Notably, in the first 20 s of H_2 flow, the intensities of the IR bands due

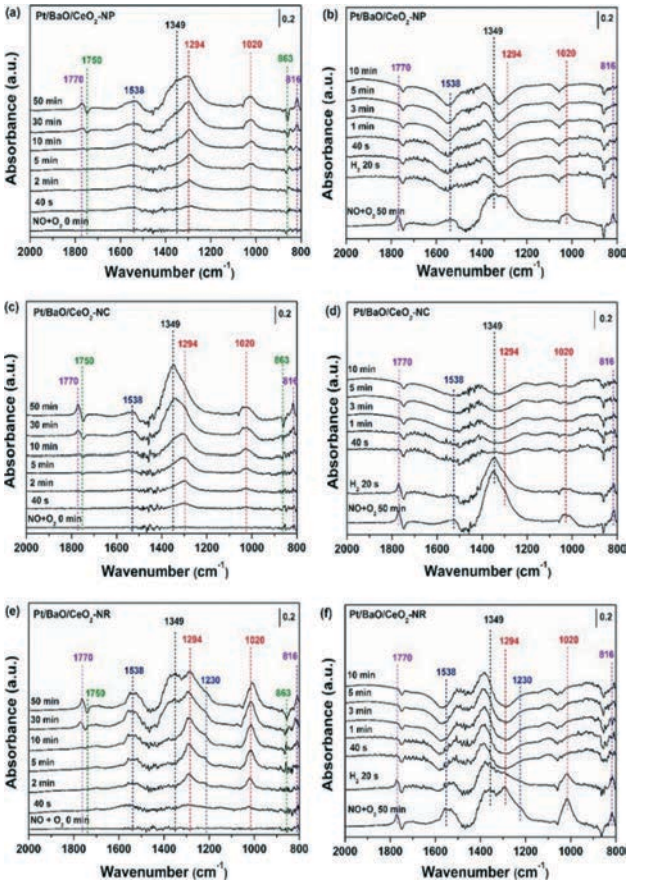

Fig. 8 *In situ* DRIFTS studies of storage (a, c, e) and reduction (b, d, f,) process at 350 °C for Pt/BaO/CeO_2-NP, Pt/BaO/CeO_2-NC and Pt/BaO/CeO_2-NR.

to nitrates adsorbed on the surface of Pt/BaO/CeO_2-NC (1538, 1294, and 1024 cm^{-1}) and free nitrate (1349 cm^{-1}) only decreased slightly, disappearing after introduction of H_2 for 1 min. As a result, it is reasonable that Pt/BaO/CeO_2-NC exhibits low activity for NO_x conversion under lean–rich cyclic conditions as shown in Fig. 4.

Obviously, bidentate nitrates on Ba sites (1020 and 1294 cm^{-1}) and monodentate nitrate on Ce sites (1538 cm^{-1}) were also formed on the surface of the Pt/BaO/CeO_2-NR catalyst (Fig. 8e). By comparing the intensities of the bands due to the two nitrate species, we can easily conclude that the Pt/BaO/CeO_2-NR catalyst possesses more adsorption sites available for NO_x storage than Pt/BaO/CeO_2-NP and Pt/BaO/CeO_2-NC. This conclusion was further confirmed by the appearance of a shoulder peak at 1230 cm^{-1} assigned to bridged bidentate nitrites on Ba or Ce sites, while it was not observed in Fig. 8a and c.[67] Also, bulk nitrates (816 and 1770 cm^{-1}) and free ions (1349 cm^{-1}) were observed after feeding of NO + O_2 for 10 min.

When Pt/BaO/CeO_2-NR was exposed to a reducing atmosphere (Fig. 8f), the bands at 1538, 1294, 1230, and 1020 cm^{-1} decreased sharply, indicating the high activity of surface nitrates and nitrate ions. After 40 s of reduction, few

adsorbed species remained on Pt/BaO/CeO_2-NR, further demonstrating its high NO_x removal efficiency as shown in Fig. 4c.

Looking back at the NO_x storage behavior (Fig. 8a, c, and e), one can easily find that, within the initial 2 min over all the NSR catalysts, the nitrates adsorbed on the surface sites of Ba (1020 and 1294 cm^{-1}) and Ce (1538 cm^{-1}) were predominant. This means that, in our lean (90 s)–rich (6 s) cyclic conditions, the availability of surface Ba and Ce sites is crucial for NO_x storage.

Relationship between the properties of the catalysts and catalytic performance

Even though all Pt/BaO/CeO_2 samples had almost the same Ba and Pt loadings, their catalytic performance for the NSR process was strongly dependent on the shape of the ceria support. The nanoparticle-based NSR catalyst exhibits a much larger BET surface area than the nanorod-related one (Table 1), while the former shows a significantly lower NSC value than the latter (Fig. 3). Also, under lean–rich conditions, the activity of Pt/BaO/CeO_2-NP for NO_x conversion is poorer than Pt/BaO/CeO_2-NR. These results show that the surface area of Pt/BaO/CeO_2 is not a determining factor for the NSR process. It also suggested that ceria can serve as a component for NO_x storage, which was identified by our *in situ* DRIFTS measurements. As shown in Fig. S9,† however, the NO_x storage capacity of ceria is marginal.

Previous studies showed that the oxidation of NO to NO_2 was crucial for the NO_x storage capacity, the occurrence of which was closely related to the presence of a noble metal. Combining the result of H_2-TPR (Fig. 7 and Table S6†) with that of NSC (Fig. 3), the larger amount of the available Pt is, the higher the NO_x storage capacity is. Over CeO_2 supported catalysts, experimental measurement and theoretical prediction confirmed that the oxygen vacancies are anchoring sites for the noble metal, creating a strong metal–support bond, thus enhancing the catalytic activity.[9,68,69] If the results presented in Fig. 6 and 7 are taken into account, it is easy to find that the higher the concentration of Ce^{3+} is, the higher the availability of Pt is. These results mentioned above suggest that the oxygen vacancies play a key role in NO_x storage over Pt/BaO/CeO_2. Furthermore, it is interesting to note that a good linear correlation between the Ce^{3+} concentrations of reduced NSR catalysts and their NO_x storage capacities was observed in the temperature range of 200–350 °C (Fig. 9a), indicating that oxygen vacancies may govern the process of NO_x storage. At temperatures above 350 °C, however, such a linear relationship was not observed between the Ce^{3+} content and NSC value. Glancing at Fig. 5, one can easily find that the stored NO_x begins to decompose at 350 °C, the occurrence of which gives a negative contribution to the NSC value of Pt/BaO/CeO_2. As a result, a linear relationship was not obtained at the high temperature of 400 °C.

As described in the previous literature, the presence of Ce^{3+} is accompanied by the formation of oxygen vacancies on the surface of ceria,[54] on which active oxygen (O*) is created.[70] A linear relationship between the Ce^{3+} concentration on the reduced NSR catalysts and the H_2 consumption of total surface CeO_2 (Fig. S12†) further suggests that the oxygen vacancies both neighbouring the Pt and far away from the Pt are active for oxygen activation.

Interestingly, there is a close linear correlation between the H_2 consumption of total surface CeO_2 and the NO_x storage capacity of different shaped ceria-based catalysts at 200–350 °C (Fig. 9b), revealing that the surface active oxygen trapped by oxygen vacancies plays a crucial role in the NO_x storage process.

As presented in Fig. S11,† however, ceria only exhibits a marginal NO_x storage capacity even though it contains large amounts of oxygen vacancies. With this in mind, a question may arise: how does the oxygen species activated by oxygen vacancies on ceria govern the NO_x storage, which is mainly trapped on Ba sites?

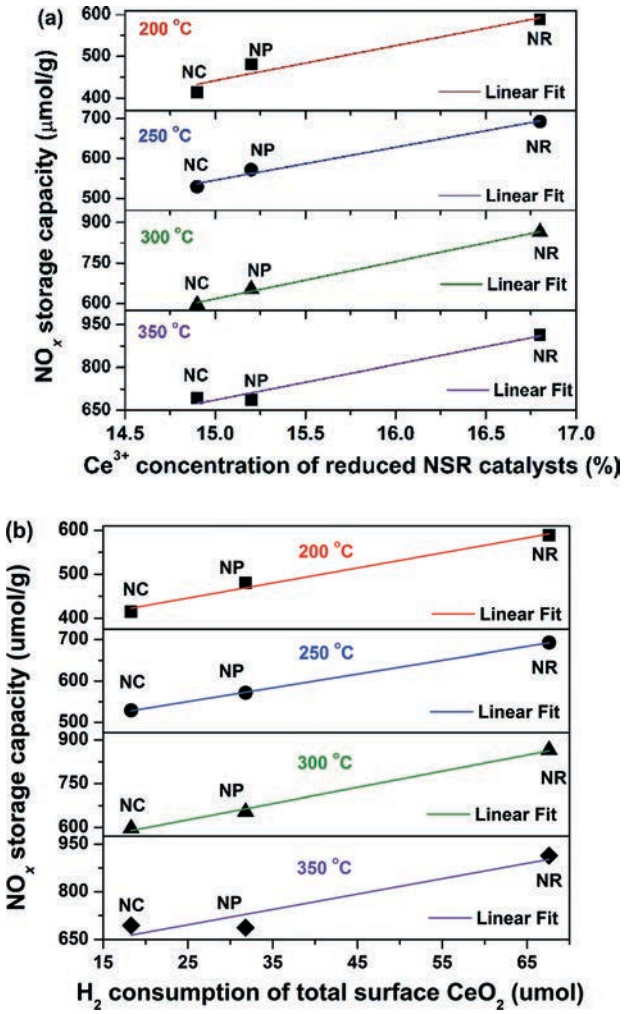

Fig. 9 The relationship between the concentration of Ce^{3+} measured by XPS and the NO_x storage capacity of all the Pt/BaO/CeO_2 catalysts (a); the relationship between the H_2 consumption of surface CeO_2 measured by H_2-TPR and the NO_x storage capacity of all the Pt/BaO/CeO_2 catalysts (b).

Among the three NSR catalysts, Pt/BaO/CeO_2-NR has the highest concentration of Ce^{3+}, and the highest number of oxygen vacancies both neighbouring the Pt and far away from the Pt, creating the largest amount of active oxygen species (eqn (1)). The O* species are active for NO_2 formation on the Pt sites (eqn (2))[71] and also for nitrate production (eqn (3)).[72] Considering that the Ba sites exhibit higher basicity than the Ce sites,[73] the produced nitrates are thus preferably stored on and/or transfer to the former, which has been established by Fig. S11 and 8.† This feature of nitrate adsorption also guarantees the availability of oxygen vacancies for further activation of O_2, nitrate formation, and further transformation of nitrate.

$$2Pt\cdots Ce^{3+}\text{-}\square + O_2 \rightarrow 2Pt\cdots Ce^{4+} - O* \quad (1)$$

$$NO + Pt\cdots Ce^{4+}\text{-}O* \rightarrow NO_2 + Pt + Ce^{3+}\text{-}\square \quad (2)$$

$$BaO + 2NO_2 + Ce^{4+} - O* \rightarrow Ba(NO_3)_2 + Ce^{3+}\text{-}\square \quad (3)$$

$$BaO + 2NO + 3Ce^{4+} - O* \rightarrow Ba(NO_3)_2 + 3Ce^{3+}\text{-}\square \quad (4)$$

where, Pt$\cdots$$Ce^{3+}$-□ represents the Pt sites neighbouring oxygen vacancies while Pt$\cdots$$Ce^{4+}$–O* means the active oxygen species adsorbed on Pt$\cdots$$Ce^{3+}$-□.

Conclusions

The CeO_2-nanorod based NSR catalyst displayed an excellent NO_x storage capacity that can reach as high as 913.8 μmol NO_x g_{cat}^{-1}, as well as high NO_x removal efficiency in periodically alternating lean–rich atmospheres (90 s *vs.* 6 s). During 20 lean–rich cycles of operation, an extraordinarily high NO_x conversion (>96.6%) was achieved on Pt/BaO/CeO_2-NR in the temperature range 200–400 °C. During the cyclic operation, this catalyst also exhibits much lower selectivity to ammonia and higher tolerance of H_2O and CO_2. XPS measurements confirm the formation of oxygen vacancies on the surface of ceria and Pt/BaO/CeO_2. A higher concentration of oxygen vacancies guarantees that large amounts of Pt species are available for NO oxidation to NO_2 over Pt/BaO/CeO_2, indicating the key role of oxygen vacancies in anchoring and dispersion of Pt. Over all the NSR catalysts, the concentration of Ce^{3+} is linearly correlated with the NO_x storage capacity. This relationship reveals that the oxygen vacancies on the ceria surface govern the formation and/or transformation of nitrates *via* the reaction between NO (and/or NO_2) and active O species created on oxygen vacancies. The superior activity of the CeO_2-nanorod-supported NSR catalyst for NO_x storage thus originates from the higher numbers of oxygen vacancies, located both neighbouring and far away from the Pt on the ceria surface.

Acknowledgements

This work was supported by the National Natural Science Foundation of China (51221892 and 21373261) and the National High Technology Research and Development Program of China (863 Program, 2013AA065301).

Notes and references

1 W. S. Epling, L. E. Campbell, A. Yezerets, N. W. Currier and J. E. Parks, *Catal. Rev.: Sci. Eng.*, 2004, **46**, 163–245.
2 Z. M. Liu and S. I. Woo, *Catal. Rev.: Sci. Eng.*, 2006, **48**, 43–89.
3 A. B. Sounak Roy, *Chem. Rev.*, 2009, **109**, 4054–4091.
4 G. Liu and P.-X. Gao, *Catal. Sci. Technol.*, 2011, **1**, 552–568.
5 Z. Hu, K. Sun and B. Xu, *Chin. J. Catal.*, 2011, **32**, 17–26.
6 Z. Hu, W.-Z. Li, K.-Q. Sun and B.-Q. Xu, *Catal. Sci. Technol.*, 2013, **3**, 2062–2071.
7 A. Trovarelli, *Catal. Rev.: Sci. Eng.*, 1996, **38**, 439–520.
8 Y. T. Kim, E. D. Park, H. C. Lee, D. Lee and K. H. Lee, *Appl. Catal., B*, 2009, **90**, 45–54.
9 Y. Li and W. Shen, *Chem. Soc. Rev.*, 2014, **43**, 1543–1574.
10 X. Wang, Y. Yu and H. He, *Appl. Catal., B*, 2011, **104**, 151–160.
11 Y. Ren and M. P. Harold, *ACS Catal.*, 2011, **1**, 969–988.
12 Z. Say, E. I. Vovk, V. I. Bukhtiyarov and E. Ozensoy, *Appl. Catal., B*, 2013, **142–143**, 89–100.
13 C. Shi, Y. Ji, U. M. Graham, G. Jacobs, M. Crocker, Z. Zhang, Y. Wang and T. J. Toops, *Appl. Catal., B*, 2012, **119–120**, 183–196.
14 Z. Say, E. I. Vovk, V. I. Bukhtiyarov and E. Ozensoy, *Top. Catal.*, 2013, **56**, 950–957.
15 D. H. Kim, J. H. Kwak, J. Szanyi, X. Wang, G. Li, J. C. Hanson and C. H. F. Peden, *J. Phys. Chem. C*, 2009, **113**, 21123–21129.
16 N. Le Phuc, X. Courtois, F. Can, S. Royer, P. Marecot and D. Duprez, *Appl. Catal., B*, 2011, **102**, 362–371.
17 R. Buechel, R. Strobel, A. Baiker and S. E. Pratsinis, *Top. Catal.*, 2009, **52**, 1709–1712.
18 Z.-Q. Zou, M. Meng, N. Tsubaki, J.-J. He, G. Wang, X.-G. Li and X.-Y. Zhou, *J. Hazard. Mater.*, 2009, **170**, 118–126.
19 M. Yang, Y. Li, J. Wang and M. Shen, *J. Catal.*, 2010, **271**, 228–238.
20 J. X. Zhu, M. Q. Shen, L. F. Lu, J. Wang and J. Q. Wang, *Acta Phys.-Chim. Sin.*, 2014, **30**(8), 1559–1566.
21 R. You, Y. Zhang, D. Liu, M. Meng, Z. Jiang, S. Zhang and Y. Huang, *Chem. Eng. J.*, 2015, **260**, 357–367.
22 M. Casapu, J. D. Grunwaldt, M. Maciejewski, M. Wittrock, U. Gobel and A. Baiker, *Appl. Catal., B*, 2006, **63**, 232–242.
23 J.-Y. Luo, W. S. Epling, G. Qi and W. Li, *Catal. Lett.*, 2012, **142**, 946–958.
24 K. F. Li Fan, *J. Catal.*, 1997, **172**, 238–242.
25 M. Piacentini, M. Maciejewski and A. Baiker, *Appl. Catal., B*, 2007, **72**, 105–117.
26 K. Zhou, X. Wang, X. Sun, Q. Peng and Y. Li, *J. Catal.*, 2005, **229**, 206–212.
27 S. Carrettin, P. Concepcion, A. Corma, J. M. Lopez Nieto and V. F. Puntes, *Angew. Chem., Int. Ed.*, 2004, **43**, 2538–2540.
28 X.-S. Huang, H. Sun, L.-C. Wang, Y.-M. Liu, K.-N. Fan and Y. Cao, *Appl. Catal., B*, 2009, **90**, 224–232.

29 R. Si and M. Flytzani-Stephanopoulos, *Angew. Chem.*, 2008, **120**, 2926–2929.
30 S. Wang, L. Zhao, W. Wang, Y. Zhao, G. Zhang, X. Ma and J. Gong, *Nanoscale*, 2013, **5**, 5582–5588.
31 R. Gao, D. Zhang, P. Maitarad, L. Shi, T. Rungrotmongkol, H. Li, J. Zhang and W. Cao, *J. Phys. Chem. C*, 2013, **117**, 10502–10511.
32 P. Maitarad, J. Han, D. Zhang, L. Shi, S. Namuangruk and T. Rungrotmongkol, *J. Phys. Chem. C*, 2014, **118**, 9612–9620.
33 W.-I. Hsiao, Y.-S. Lin, Y.-C. Chen and C.-S. Lee, *Chem. Phys. Lett.*, 2007, **441**, 294–299.
34 G. Yi, Z. Xu, G. Guo, K.-i. Tanaka and Y. Yuan, *Chem. Phys. Lett.*, 2009, **479**, 128–132.
35 L.-D. S. Hao-Xin Mai, Y.-W. Zhang, R. Si, W. Feng, H.-P. Zhang and C.-H. Y. Hai-Chao Liu, *J. Phys. Chem. B*, 2005, **109**, 24380–24385.
36 J. W. Cook, *J. Appl. Phys.*, 1981, **52**, 5024.
37 M. Valden, *Science*, 1998, **281**, 1647–1650.
38 L. W. Zhong and X. D. Feng, *J. Phys. Chem. B*, 2003, **107**, 13563–13566.
39 X. Wang, Z. Jiang, B. Zheng, Z. Xie and L. Zheng, *CrystEngComm*, 2012, **14**, 7579–7582.
40 J. A. Anderson, B. Bachiller-Baeza and M. Fernandez-Garcia, *Phys. Chem. Chem. Phys.*, 2003, **5**, 4418–4427.
41 E. Fridell, H. Persson, B. Westerberg, L. Olsson and M. Skoglundh, *Catal. Lett.*, 2000, **66**, 71–74.
42 Z. Say, M. Dogac, E. I. Vovk, Y. E. Kalay, C. H. Kim, W. Li and E. Ozensoy, *Appl. Catal., B*, 2014, **154–155**, 51–61.
43 X. Wang, Y. Yu and H. He, *Appl. Catal., B*, 2010, **100**, 19–30.
44 N. Le Phuc, X. Courtois, F. Can, S. Royer, P. Marecot and D. Duprez, *Appl. Catal., B*, 2011, **102**, 353–361.
45 L. Olsson and E. Fridell, *J. Catal.*, 2002, **210**, 340–353.
46 V. K. Kaushik, *Z. Phys. Chem.*, 1991, **173**, 105–113.
47 Y. Nagai, T. Hirabayashi, K. Dohmae, N. Takagi, T. Minami, H. Shinjoh and S. Matsumoto, *J. Catal.*, 2006, **242**, 103–109.
48 S. Hosokawa, M. Taniguchi, K. Utani, H. Kanai and S. Imamura, *Appl. Catal., A*, 2005, **289**, 115–120.
49 T. H. Seiichiro Imamura, Y. Saito, H. Aritani, H. Kanai, Y. Matsumura and N. Tsuda, *Catal. Today*, 1999, **50**, 369–380.
50 A. Casapu, J. D. Grunwaldt, M. Maciejewski, F. Krumeich, A. Baiker, M. Wittrock and S. Eckhoff, *Appl. Catal., B*, 2008, **78**, 288–300.
51 T. F. S. Tsunekawa and A. Kasuya, *Surf. Sci.*, 2000, **457**, L437–L440.
52 S. Mahammadunnisa, P. Manoj Kumar Reddy, N. Lingaiah and C. Subrahmanyam, *Catal. Sci. Technol.*, 2013, **3**, 730–736.
53 S. A. Acharya, V. M. Gaikwad, S. W. D'Souza and S. R. Barman, *Solid State Ionics*, 2014, **260**, 21–29.
54 K. Z. Xiangwen Liu, L. Wang, B. Wang and Y. Li, *J. Am. Chem. Soc.*, 2009, **131**, 3140–3141.
55 S. Chang, M. Li, Q. Hua, L. Zhang, Y. Ma, B. Ye and W. Huang, *J. Catal.*, 2012, **293**, 195–204.
56 J. P. Faical Larachia, A. Adnot and Al. Bernis, *Appl. Surf. Sci.*, 2002, **195**, 236–250.
57 M. Nolan, S. C. Parker and G. W. Watson, *Surf. Sci.*, 2005, **595**, 223–232.
58 C. B. Ahmed Badri and J.-C. Lavalley, *J. Chem. Soc., Faraday T rans.*, 1997, **93**, 1159–1168.
59 M. Tamura and K. Tomishige, *Angew. Chem., Int. Ed.*, 2015, **54**, 864–867.
60 Z. Wu, M. Li, D. R. Mullins and S. H. Overbury, *ACS Catal.*, 2012, **2**, 2224–2234.
61 N. Acerbi, S. Golunski, S. C. Tsang, H. Daly, C. Hardacre, R. Smith and P. Collier, *J. Phys. Chem. C*, 2012, **116**, 13569–13583.
62 N. Acerbi, S. C. Tsang, G. Jones, S. Golunski and P. Collier, *Angew. Chem., Int. Ed.*, 2013, **52**, 7737–7741.
63 B. W. Louise Olsson, H. Persson, E. Fridell, M. Skoglundh and B. Andersson, *J. Phys. Chem. B*, 1999, **103**, 10433–10439.
64 T. Szailer, J. H. Kwak, D. H. Kim, J. C. Hanson, C. H. F. Peden and J. Szanyi, *J. Catal.*, 2006, **239**, 51–64.
65 L. Lv, X. Wang, M. Shen, Q. Zhang and J. Wang, *Chem. Eng. J.*, 2013, **222**, 401–410.
66 T. J. Toops, D. B. Smith and W. P. Partridge, *Appl. Catal., B*, 2005, **58**, 245–254.
67 E. F. BjörnWesterberg, *J. Mol. Catal. A: Chem.*, 2001, **165**, 249–263.
68 H. Y. Kim, H. M. Lee and G. Henkelman, *J. Am. Chem. Soc.*, 2012, **134**, 1560–1570.
69 J. A. Farmer and C. T. Campbell, *Science*, 2010, **329**, 933–936.
70 Q. Liang, X. Wu, D. Weng and H. Xu, *Catal. Today*, 2008, **139**, 113–118.
71 G. Qi and W. Li, *Catal. Today*, 2012, **184**, 72–77.
72 X.-G. Li, Y.-H. Dong, H. Xian, W. Y. Hernandez, M. Meng, H.-H. Zou, A.-J. Ma, T.-Y. Zhang, Z. Jiang, N. Tsubaki and P. Vernoux, *Energy Environ. Sci.*, 2011, **4**, 3351–3354.
73 A. S. Ivanova, *Kinet. Catal.*, 2005, **46**, 620–633.

